JOURNAL OF PROPULSION AND POWER
Vol. 21, No. 3, May–June 2005

Analysis of Magnetohydrodynamic Generator Power Generation

Ding Li,* Dennis Keefer,† Robert Rhodes,‡ Charles L. Merkle,§ and Konstantin Kolokolnikov¶
University of Tennessee Space Institute, Tullahoma, Tennessee 37388
and
Rene Thibodeaux**
U.S. Air Force Research Laboratory, Dayton, Ohio 45433-7251

The three-dimensional current and fluid flow characteristics of diagonally connected magnetohydrodynamics generators are studied by means of numerical solutions. The formulation solves the Navier–Stokes equations in conjunction with the magnetic diffusion equation and a two-equation turbulence model on a hybrid unstructured grid. The current is obtained from Ampere's law, and a generalized Ohm's law is used to include the Hall effect. A flux-split upwind discretization is used for the convective terms along with a nonconservative correction that drives the divergence of the magnetic field to zero. Physical difficulties with boundary conditions are removed by extending the computational domain into the far field to encompass the plasma channel, the conducting and dielectric walls, and the surrounding air. The fluid flow and magnetic field solvers can be updated in loosely or closely coupled fashion depending on the magnetic Reynolds number. Results are shown for supersonic flow generators with both constant and diverging area channels. Properties are based on equilibrium table lookup for combustion gas products with potassium seedant.

Nomenclature

A_i	=	cell face area
A_n, A_{nc}	=	conservative and nonconservative flux Jacobians
$\bar{\boldsymbol{B}}$, $\boldsymbol{E}$	=	magnetic flux density and electric field vector
c, c_A, $c_{f,s}$	=	speed of sound in the fluid, Alfven wave speed, and fast and slow magnetoacoustic speeds
e, n	=	electron charge and electron number density
$\boldsymbol{F}$, $\boldsymbol{F}_V$	=	inviscid and viscous flux vectors
h^0, h_B^0	=	total enthalpy without and with magnetic pressure
$\bar{\boldsymbol{J}}$	=	electric current density, (J_x, J_y, J_z)
$\boldsymbol{n}$	=	surface normal vector, (n_x, n_y, n_z)
$\boldsymbol{Q}$, $\boldsymbol{Q}_p$	=	vectors of conservative and primitive variables
$\boldsymbol{V}$	=	velocity vector, (u, v, w)
Y_k	=	mass fraction of species k
Γ	=	time-derivative Jacobian matrix
μ, λ	=	fluid viscosity and thermal conductivity
μ_0	=	vacuum permeability
σ	=	electrical conductivity

Introduction

MAGNETOHYDRODYNAMIC (MHD) generators use the flow of an ionized gas through a magnetic field to produce electrical power. Although several classical geometrical configurations are available, the gas typically passes through a flow channel in the generator that is composed of individual sections of high electrical conductivity separated from each other by insulating, dielectric sections. The particular arrangement of the conductor/dielectric sections distinguishes the types of MHD generator and their ensuing electrical output characteristics.[1] Electrical leads attached to conducting sections on opposite sides or ends of the generator are used to extract power from the channel and to connect it to a useful external load.

A characteristic of MHD generators is that the combined electromagnetic (EM) and hydrodynamic fields are highly complex and inherently three dimensional in nature. The focus of the present paper is to identify some of the detailed physics of channel operation, including the effects of nonideal current distribution in the electrodes and plasma, the cross-channel current paths, and local effects near the conductor/insulator interfaces, along with details of the three-dimensional flowfield. Our approach is based on detailed three-dimensional solutions of the magnetic diffusion equations and the Reynolds averaged Navier–Stokes equations.

The specific problem of interest is a diagonally connected MHD channel surrounded by a magnet. Supersonic flow enters the channel from one end and exits through the other. The air is seeded with potassium to provide electrical conductivity. The channel is composed of a series of conducting regions separated from each other by strips of insulator stacked along the channel and oriented at an angle with respect to the axis. An external load is impressed across the ends of the channel allowing current to be extracted from the flow. The multiple diagonal sections in combination with the electrically conducting plasma give the advantage of increased output voltage through an effectively series connection. Representative conditions of interest involve low magnetic Reynolds numbers and Hall parameters of order unity.

In the following sections, we first present the model formulation and outline the numerical solution procedure. Following this we describe the geometry of the diagonally connected generator and related configurations that are used for the present calculations. Representative results are presented in the final section, starting with a brief validation comparison against solutions from an independent code, followed by a series of simulations of the combined EM–fluid dynamic fields in MHD generators.

Problem Formulation

The computational model is based on an unstructured grid, time-marching code[2,3] that solves both the Navier–Stokes equations and the magnetic diffusion equation with the current determined from Ampere's law. The equations are solved by means of conventional flux-difference split upwind methods. The divergence of the magnetic field is included in the equations following Powell et al.[4,5]

Presented as Paper 2003-5050 at the AIAA/ASME/SAE/ASEE 39th Joint Propulsion Conference and Exhibit, Huntsville, AL, 20 July 2003; received 6 August 2003; revision received 28 September 2004; accepted for publication 24 October 2004. Copyright © 2004 by the American Institute of Aeronautics and Astronautics, Inc. All rights reserved. Copies of this paper may be made for personal or internal use, on condition that the copier pay the $10.00 per-copy fee to the Copyright Clearance Center, Inc., 222 Rosewood Drive, Danvers, MA 01923; include the code 0748-4658/05 $10.00 in correspondence with the CCC.

*Research Associate Professor, MAES. Member AIAA.
†Professor, MAES. Member AIAA.
‡Research Professor, MAES. Member AIAA.
§Professor, H. H. Arnold Chair in Computational Mechanics. Senior Member AIAA.
¶MS Candidate, MAES.
**Research Scientist, Power Division. Member AIAA.

and is forced to zero as the computation converges. Turbulence is modeled by a k, ω two-equation model.[6] Species concentration and diffusion equations are used to determine the local concentration of the potassium seed. In the present computations, the resulting electrical conductivity of the plasma is modeled as a constant or in an equilibrium fashion. More detailed electrical conductivity models can be included but are not expected to alter the global features of the solutions.

For convenience, the magnetic field is split into a known impressed field plus an unknown perturbation that is obtained from the MHD-flow computation. The conductivities in the conductors and insulators are treated as constants that are input at startup. Computations to date have routinely used conductivity ratios of 10^{10} between conductor and insulator.

Governing Equations

The governing equations of real MHD flows describe the physics of a plasma including the Hall effect. The MHD system comprises a set of conservation equations for mass, species mass fraction, momentum, and energy, along with the magnetic induction equation. These conservation equations are complemented by Ampere's law, a generalized Ohm's law, and a set of thermodynamic relations. The conservation equations are

$$\frac{\partial \rho}{\partial t} + \nabla \cdot (\rho v \boldsymbol{V}) = 0 \tag{1}$$

$$\frac{\partial \rho Y}{\partial t} + \nabla \cdot (\rho Y \boldsymbol{V}) = \nabla \cdot \rho D \nabla Y \tag{2}$$

$$\frac{\partial \rho \boldsymbol{V}}{\partial t} + \nabla \cdot (\rho \boldsymbol{V}\boldsymbol{V} + p\boldsymbol{I}) = \nabla \cdot \boldsymbol{\tau} + \boldsymbol{J} \times \boldsymbol{B} \tag{3}$$

$$\frac{\partial (\rho h_0 - p)}{\partial t} + \nabla \cdot (\rho h_0 \boldsymbol{V}) = -\nabla \cdot \boldsymbol{q} + \Delta \cdot (\boldsymbol{\tau} \cdot \boldsymbol{v}) + \boldsymbol{J} \cdot \bar{E} \tag{4}$$

$$h_B^0 = h^0 + (\boldsymbol{B} \cdot \boldsymbol{B})/2\rho\mu_0 \tag{5}$$

where $Y = (Y_1, Y_2, \ldots, Y_K,)$ is the species mass fraction, the vectors $\bar{\boldsymbol{B}} = (B_x, B_y, B_z)$ and $\bar{\boldsymbol{E}} = (E_x, E_y, E_z)$ are the magnetic flux density and the electric field, and $\bar{J} \times \bar{B}$ and $\bar{J} \cdot \bar{E}$ are the Lorentz force and the electrical power dissipation. The heat flux vector $\bar{\boldsymbol{q}}$ is expanded as

$$\boldsymbol{q} = -\lambda \nabla T + \rho D h \nabla Y \tag{6}$$

The conservation equations are complemented by a generalized Ohm's law, Ampere's law, and a set of property relations including an equation of state, an enthalpy relation, a state-dependent electrical conductivity, and the electron number density and transport properties,

$$\boldsymbol{E} = -\boldsymbol{V} \times \boldsymbol{B} + (1/\sigma)\boldsymbol{J} + (1/ne)\boldsymbol{J} \times \boldsymbol{B} \tag{7}$$

$$\boldsymbol{J} = (1/\mu_0)\nabla \times \boldsymbol{B} \tag{8}$$

$$\rho = \rho(p, T, Y_k), \qquad h = h(p, T, Y_k), \qquad \sigma = \sigma(p, T, Y_k)$$

$$n = n(p, T, Y_k), \qquad \mu = \mu(p, T, Y_k), \qquad \lambda = \lambda(p, T, Y_k) \tag{9}$$

Coupled Vector System

When a generalization of the vector formulations introduced in Refs. 4 and 5 is used, the conservation equations can be expressed as a coupled vector system that includes both conservative and nonconservative terms:

$$\Gamma \frac{\partial \boldsymbol{Q}_p}{\partial t} + \nabla \cdot (\boldsymbol{F} - \boldsymbol{F}_v) + A_{nc} \nabla \cdot \boldsymbol{Q} = 0 \tag{10}$$

Here, the vectors of conservative and primitive variables are defined as

$$\boldsymbol{Q} = \begin{bmatrix} \rho \\ \rho Y \\ \rho \boldsymbol{v} \\ \rho h_B^0 - p \\ \boldsymbol{B} \end{bmatrix}, \qquad \boldsymbol{Q}_p = \begin{bmatrix} p \\ Y \\ \boldsymbol{v} \\ T \\ \boldsymbol{B} \end{bmatrix} \tag{11}$$

The time-derivative matrix, $\Gamma = \partial \boldsymbol{Q}/\partial \boldsymbol{Q}_p$, is given by the Jacobian

$$\Gamma = \begin{bmatrix} \rho_p & \rho_Y & 0 & \rho_T & 0 \\ \rho_p Y & \rho_Y Y + \rho & 0 & \rho_T Y & 0 \\ \rho_p \boldsymbol{v} & \rho_Y \boldsymbol{v} & \rho I & \rho_T \boldsymbol{v} & 0 \\ \rho_p h_0 + & & & & \\ \quad \rho h_p - 1 & \rho_Y h_0 + \rho h_Y & \rho \boldsymbol{v}^T & \rho_T h_0 + \rho h_T & \boldsymbol{B}^T/\mu_0 \\ 0 & 0 & 0 & 0 & I \end{bmatrix} \tag{12}$$

and the conservative portion of the convective flux vector is

$$\boldsymbol{F} = \begin{bmatrix} \rho \boldsymbol{v} \\ \rho \boldsymbol{v} Y \\ \rho \boldsymbol{v}\boldsymbol{v} - \dfrac{1}{\mu_0}\boldsymbol{B}\boldsymbol{B} + p_B \boldsymbol{I} \\ h_B^0 \, \boldsymbol{v} - \dfrac{1}{\mu_0}(\boldsymbol{v} \cdot \boldsymbol{B})\boldsymbol{B} \\ \boldsymbol{v}\boldsymbol{B} - \boldsymbol{B}\boldsymbol{v} \end{bmatrix} \tag{13}$$

In these expressions, we have defined

$$p_B = p + (\bar{B} \cdot \bar{B})/2\mu_0 \tag{14}$$

$$h_B^0 = h^0 + (\bar{B} \cdot \bar{B})/2\mu_0 \tag{15}$$

The coefficient matrix of the nonconservative portion of the convective term is

$$A_{nc} = \frac{1}{\mu_0} \begin{pmatrix} 0 & 0 & 0 & 0 & 0 \\ 0 & 0 & 0 & 0 & 0 \\ 0 & 0 & 0 & 0 & \boldsymbol{B} \\ 0 & 0 & 0 & 0 & \boldsymbol{V} \cdot \boldsymbol{B} \\ 0 & 0 & 0 & 0 & \boldsymbol{V}\mu_0 \end{pmatrix} \tag{16}$$

Finally, the vector form of the viscous flux is

$$\boldsymbol{F}_v = \begin{matrix} 0 \\ \rho D Y \\ (\boldsymbol{\tau}) \\ (\boldsymbol{\tau} \cdot \boldsymbol{V}) - \boldsymbol{q} - \dfrac{1}{\mu_0^2}\left\{\dfrac{1}{\sigma}[(\nabla \times \boldsymbol{B}) + (\nabla \times \boldsymbol{B}) \times \boldsymbol{B})] \times \boldsymbol{B}\right\} \\ (\boldsymbol{\pi}) \end{matrix} \tag{17}$$

where $\boldsymbol{\tau}$ and $\boldsymbol{\pi}$ are the molecular stress and the resistivity tensor, respectively,

$$\boldsymbol{\tau} = 2\mu\left(\boldsymbol{S} - \frac{1}{3}\boldsymbol{S}I\right), \qquad S_{ij} = \left(\frac{\partial u_i}{\partial x_j} + \frac{\partial u_j}{\partial x_i}\right)$$

$$\nabla \cdot \boldsymbol{\pi} = -\nabla \times \left(\frac{1}{\sigma\mu_0}\nabla \times B\right) - \nabla \times \left(\frac{1}{\mu_0 ne} J \times B\right) \tag{18}$$

Eigenvalues and Eigenvectors of the Combined Fluids–EM System

When primitive variables are used, Eq. (10) may be rewritten as

$$\frac{\partial \boldsymbol{Q}_p}{\partial t} + \Gamma^{-1}(\boldsymbol{A}_n + \boldsymbol{A}_{nc})\nabla \boldsymbol{Q}_p = \Gamma^{-1}\nabla \cdot \boldsymbol{F}_v \tag{19}$$

where $\boldsymbol{A}_n = \partial \boldsymbol{F}/\partial \boldsymbol{Q}_p$ represents the flux Jacobian. To implement a Riemann solver on an arbitrary mesh, it is necessary to project these matrices to a general direction, $\boldsymbol{n} = (n_x, n_y, n_z)$,

$$\Gamma^{-1}(A_n + A_{nc}) = \begin{pmatrix} U & 0 & \dfrac{\rho^2 h_T}{\Delta}\boldsymbol{n} & 0 & \boldsymbol{0} \\ 0 & U & \boldsymbol{0} & 0 & \boldsymbol{0} \\ \dfrac{\boldsymbol{n}}{\rho} & 0 & U\boldsymbol{\delta} & \boldsymbol{0} & \dfrac{\boldsymbol{nB} - (\boldsymbol{B}\cdot\boldsymbol{n})\boldsymbol{\delta}}{\rho\mu_0} \\ 0 & 0 & \dfrac{\rho(1-\rho h_p)}{\Delta}\boldsymbol{n} & U & \boldsymbol{0} \\ \boldsymbol{0} & \boldsymbol{0} & \boldsymbol{Bn} - (\boldsymbol{B}\cdot\boldsymbol{n})\boldsymbol{\delta} & \boldsymbol{0} & U\boldsymbol{\delta} \end{pmatrix} \tag{20}$$

The nine eigenvalues of this matrix are given in Refs. 4, 5, and 7. After generalizing to an arbitrary direction, they become three particle waves, $\lambda_{1,2,3} = U$; two Alfven waves, $\lambda_{4,5} = U \pm c_N$; and four magnetoacoustic waves, $\lambda_{6,7,8,9} = U \pm c_{f,s}$. Here $U = \boldsymbol{V}\cdot\boldsymbol{n}$ is the velocity component in the normal direction, $c_n^2 = (\boldsymbol{B}\cdot\boldsymbol{n})^2/\rho\mu_0$ is the corresponding Alfven wave speed, and the fast and slow magnetoacoustic speeds are

$$c_{f,s}^2 = \frac{1}{2}\left\{c_B^2 \pm \sqrt{c_B^4 - \frac{4h_T(\boldsymbol{B}\cdot\boldsymbol{n})^2}{\Delta\mu_0}}\right\}$$

The parameter c_B represents the sum of the squares of the sound speed of the fluid and the Alfven speed, $c_B^2 = c^2 + c_A^2$. The isentropic sound speed (in the absence of a magnetic field) is $c^2 = \rho h_T/\Delta$, where $\Delta = \rho\rho_P h_T + \rho_T(1-\rho h_P)$, whereas the Alfven speed is $\boldsymbol{c}_A = \boldsymbol{B}/\sqrt{\rho\mu_0}$ or $c_A^2 = (\boldsymbol{B}\cdot\boldsymbol{B})/\rho\mu_0$. The eigenvectors of the matrix in Eq. (20) are given in Ref. 7. Their extension to a general direction is given in the Appendix.

Numerical Discretization

For the MHD power generator configurations of interest, the magnetic Reynolds number, $\sigma\mu_0 UL$, is less than 10^{-2}. Low magnetic Reynolds numbers imply that diffusion dominates the magnetic field so that it is possible to solve the magnetic and fluid dynamic equations in a loosely coupled fashion using the source terms given in Eqs. (1–7). Alternatively, the equations can be solved in a closely coupled fashion such as that suggested by Eq. (10) giving more generality for applications at higher magnetic Reynolds numbers. In the present work, we have formulated both approaches for implementation into an existing unstructured, finite volume code.[2]

For either approach, the discretized equations can be obtained by applying Stoke's and Green's theorem to Eq. (10) in each cell,

$$\iiint\left[\frac{\partial \boldsymbol{Q}}{\partial t} + \nabla\cdot(\boldsymbol{F} - \boldsymbol{F}_v)\right]\mathrm{d}\Omega = \iiint A_{nc}\nabla\cdot\boldsymbol{Q}\,\mathrm{d}\Omega \tag{21}$$

where Ω is a domain closed by surface $\delta\Omega$ and $\boldsymbol{n} = (n_x, n_y, n_z)$, is the surface normal vector. The result gives the discrete linear equation system:

$$\bar{\Gamma}\frac{\partial \bar{\boldsymbol{Q}}_p}{\partial t}V_\Omega + \sum_i^N \boldsymbol{F}_{n,i}^{\mathrm{inv}}A_i - \sum_i^N \boldsymbol{F}_{vn,i}^{\mathrm{vis}}A_i = \bar{A}_{nc}\bar{\nabla}\cdot\bar{\boldsymbol{Q}}V_\Omega \tag{22}$$

The summation is over all faces of the volume V_Ω, and A_i is the area of the ith face of the cell.

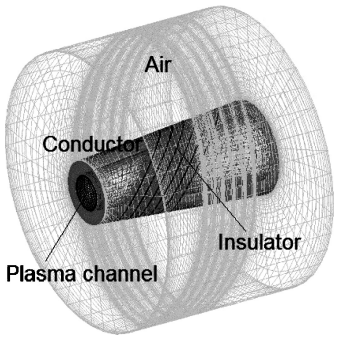

Fig. 1 Computational domain for magnetic induction equation with unstructured hexahedral grid.

Computational Domain and Boundary Conditions

The MHD system requires the specification of appropriate boundary conditions for both the fluid and the electromagnetic portions of the combined field. The spatial extent of these two fields, however, is very different. The flowfield is constrained by the channel walls to lie completely within the channel, whereas the electromagnetic field extends over all space including the plasma, the channel walls, and the exterior of the channel where the induced B field decays to zero at infinity. These very different physical domains must be reflected in both the computational domain and the boundary conditions. Accordingly, distinct computational domains are used for the fluid dynamic and MHD fields, and the corresponding boundary conditions are enforced at different locations as suggested in Fig. 1.

The computational domain for the fluid lies within the interior of the channel, and appropriate boundary conditions are enforced on its periphery. Because the present solutions are supersonic, inflow and outflow conditions are determined by specifying a complete set of flow variables at the inlet and extrapolating all variables at the outlet. The traditional no-slip condition is specified at the channel walls along with a constant wall temperature. The pressure is obtained from the normal momentum equation.

The computational domain for the magnetic field requires more explanation. Although the well-known conditions at the surface of pure insulators (zero normal current and jump in tangential current) and conductors (jump in normal magnetic field and continuous tangential field) are sometimes used to obtain boundary conditions for simple problems, it is impossible to determine a priori the magnetic field boundary conditions at a channel wall that consists of finite-valued conductors and insulators with a complex current distribution in the channel.

To circumvent this difficulty, we place the magnetic boundary conditions for the induced field on a distant surface external to the outer channel walls. The boundary conditions for the induction equation are then obtained by choosing a cylindrical domain whose radius is large compared to the flow channel and whose ends extend beyond the channel in both directions as shown in Fig. 1. Using the integral form of Ampere's law consistent with MHD assumptions (no displacement current)

$$\oint B\cdot\mathrm{d}l = \oiint \mu_0 J\cdot n\,\mathrm{d}A \tag{23}$$

we can calculate the value of the magnetic field on this cylinder. To obtain an approximate far-field boundary condition, we envision an annular current sheet starting far upstream of the channel and entering the end wall of the channel with a uniform current density and total current I. A similar uniform distribution and downstream continuation is assumed at the channel exit. Ampere's law is applied to a plane surface perpendicular to the channel axis and bounded by the intersection with the cylinder. Because the current is continuous, the term on the right is a constant of value $\mu_0 I$ for any radius outside the outer surface of the physical channel. This is true regardless of the complexity of the current distribution within the channel and yields the azimuthal component of the induced magnetic field, $B_\theta = \mu I/2\pi r$. This condition is applied on the curved and plane surfaces of the magnetic field computational domain at radii greater than the outer channel radius. The uniformity of the

current I upstream and downstream is assured by application of Ampere's law over the annular conductor.

Inside the inner radius of the conductor, there is no current, and the boundary condition there is zero. Within the complex current distribution in the flow channel, radial and azimuthal current components will give rise to axial and radial components of magnetic field; however, due to continuity of the axial current, these components tend to cancel, and the Biot–Savart law shows that they decay with the square of the radius. Therefore, on the cylindrical surface of the magnetic computational domain, axial and radial components are set to zero. In placing the external boundary conditions, we first computed a smaller field with the outer boundary set at two channel radii and then repeated the calculation with the boundary at four radii. The differences in the resulting solution were small, and all results in the paper are for the external boundary condition placed at four radii.

A second complexity in the magnetic field solution arises from the presence of material discontinuities inside the domain, for example, plasma/channel wall, channel wall/external air, and conductor/dielectric. At these interfaces, the B and J fields have two values (B^+, B^-, etc.) related to the two media. In the present calculation, we have captured these jumps by smearing the discontinuities over a thin region of a few grid cells. Efforts to fit these discontinuities and to incorporate end corrections in our external field analysis are underway but not included here.

As a final step in specifying the problem, the output voltage of the MHD generator is determined parametrically by specifying the generator current (which then gives the far-field boundary conditions), computing the field solutions and the voltage distribution, and then back calculating the load resistance required to generate this current. In parametric fashion, this gives the current–voltage load response of the generator.

Numerical Results

The operational characteristics of diagonally connected generators that form the basis for the results presented herein are given in Fig. 2. Figure 2 shows a constant area tube that is composed of alternate sections of conductor (dark) and dielectric (light) that serves as the flow channel. In the following discussion, calculations are presented for both constant area and diverging channels. The plasma enters the channel from the left end and exits at the right. The current shown in Fig. 2 also enters from the left, proceeds through the channel and exits on the right. Note that the inlet boundary for the current is farther to the left than that for the flow, as noted earlier.

As the current enters the left end of the channel, nearly all of it flows through the conductor until it comes to the first dielectric section, at which point it flows tangentially around the conductor to its downstream-most extent. Then, at this point, the low conductivity of the dielectric forces it to enter the plasma, whose conductivity lies between that of the conductor and the insulator. Once inside the plasma, the current travels across the channel, as indicated by the

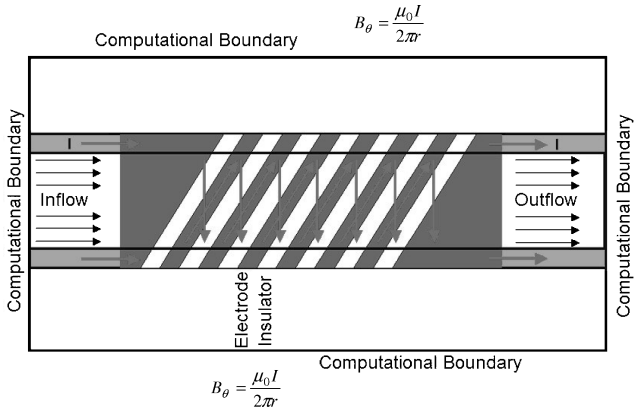

Fig. 2 Diagonally connected generator with computational domain for induction equation and fluids equations, along with global current paths.

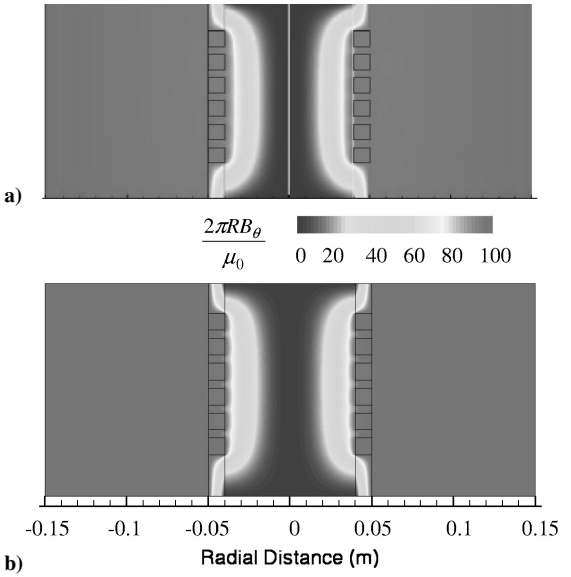

Fig. 3 Comparison of axial current density distribution in conductivity channel with six ceramic rings: a) MACH2, axisymmetric calculation, and b) GEMS, three dimensional.

arrows, to a conducting section on the opposite side of the channel. When it enters this conductor, the current travels circumferentially around the conductor until it reaches the top, where it is again forced into the plasma to repeat the process. At the downstream end, the longer conducting section collects all of the current, eventually transferring to an external load.

As verification of the magnetic field portion of the computational model, a series of test cases of increasing complexity has been calculated. Validation comparisons have been made with analytical theory and the results of existing codes, that is, MACH2 (Ref. 8) and MGMHD (Ref. 9), for cases such as a simple line conductor, a Faraday channel, and a conductivity channel with a single dielectric ring. Here we present comparisons between computations with the GEMS code and results from the MACH2 code for an axisymmetric conductivity channel with six dielectric rings. Extensive validations of the fluid dynamics portion of the computational model have also been done with representative comparisons presented elsewhere.[2,3]

The geometry of the axisymmetric channel is given in Fig. 3, along with the current distribution in the plane containing the axis of symmetry. The geometry consists of six ceramic rings 1 cm in thickness separated by 0.5-cm-thick graphite electrodes. The plasma inside the channel is stationary and has a constant conductivity of 15 mho/m. A uniform current of 100 A passes into one end of the channel and exits the opposite end. After the current enters the graphite electrode, it is forced out into the plasma by the dielectric rings, then partially returns again between insulators before finally exiting through the graphite on the opposite end.

The current distribution in Fig. 3a shows the MACH2 results and Fig. 3b the GEMS results. The MACH2 computations are axisymmetric and take advantage of the symmetry in the problem to give a precise solution that can serve as a standard. The GEMS calculations are completely three dimensional and based on a Cartesian grid to give a more critical evaluation of the capability for computing fully three-dimensional problems such as those given later. The full channel (both halves) was computed with GEMS without imposing symmetry at the centerline. As can be seen from Fig. 3, the current and electric field distributions obtained from the three-dimensional GEMS solution are similar to those from MACH2. The current density in the intermediate electrodes in the three-dimensional GEMS solution is slightly different from that obtained in the axisymmetric MACH2 calculations, but is clearly qualitatively correct. Improved comparisons can be obtained by using finer grids, but the present grid is commensurate with the ones used in the results shown later. Clearly the accuracy is sufficient to obtain insight into the detailed characteristics of the generator problem. In summary, we note that

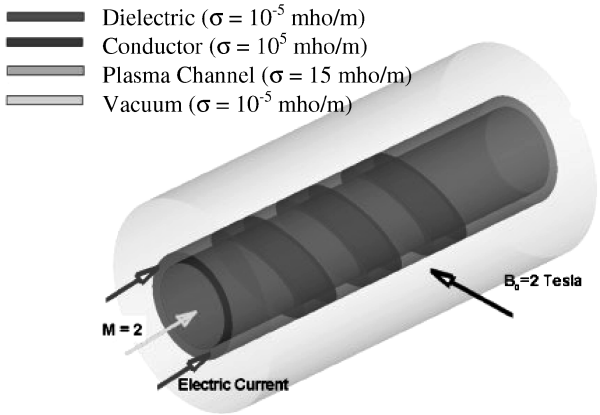

Fig. 4 Geometry of diagonally connected MHD channel with three dielectric sections at −30 deg from perpendicular: darkest portion indicates dielectric, next darkest indicates conducting section, and gray portion outside the channel indicates surrounding air.

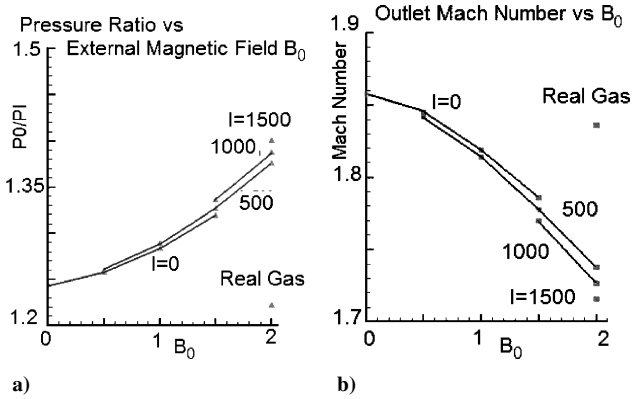

Fig. 5 Function of external magnetic field and load current with results for Saha-dependent conductivity: a) pressure ratio across MHD channel and b) outlet Mach number.

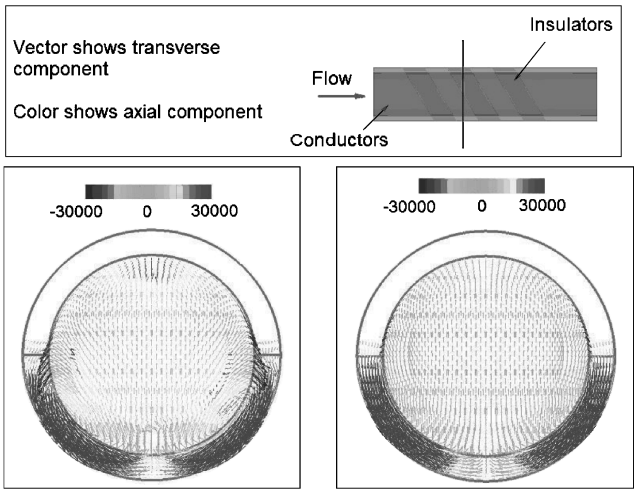

Fig. 6 Current density in plasma and channel wall at axial location $z = -0.2$ m, $B = 2$ T, $I = 1500$ A: left, constant conductivity, 15 mho/m and right, equilibrium conductivity.

the MACH2 code is a nonviscous MHD code and would not simulate the effects of boundary layers in the plasma. The GEMS simulations include detailed effects of the flowfield, including the turbulent boundary layers.

In the following sections we present results for a generator with a constant area channel and a conductivity channel with a diverging area. Generator calculations are presented for both a constant conductivity plasma and one in which the conductivity is a function of plasma properties. The conductivity channel calculations are for variable conductivity.

Constant Area MHD Generator

The geometrical configuration and computational domain used in the MHD generator calculations are shown in Fig. 4. We consider a constant area channel with three dielectric rings (shown as darkest portion in Fig. 4) oriented at an angle of −30 deg from the perpendicular. This simple configuration was chosen to evaluate the code and does not represent a practical generator configuration. An electrical current and a supersonic flow at Mach 2 enter from the left and flow through the channel. An external magnetic field of $2T$ is placed perpendicular to the channel. The conductivity in the conductor was taken as 10^5 mho/m, whereas that in the dielectric was 10^{-5}.

Computations are compared for two cases. In the one, the plasma conductivity was fixed at 15 mho/m, whereas in the second it was taken as the equilibrium ionization of a 1% concentration of potassium added to the fluid. In both cases, the physical and transport properties of the working fluid were obtained from equilibrium calculations of the combustion gases produced by a MAPP-gas/oxygen flame that were incorporated into the computations by means of a table lookup procedure. In both calculations, the fluid dynamics and the magnetic field are mutually coupled. In the first, the electrical properties of the fluid were independent of the local thermodynamic state, whereas in the second the conductivity is coupled to the MHD solution and varies strongly with the local density and temperature of the fluid. The 15 mho/m conductivity used for the constant conductivity computations corresponds to a fluid temperature of nearly 3000 K at a 1% potassium concentration. As a result, the conductivity in the equilibrium calculations is considerably lower than that in the constant conductivity case. The Hall parameter Φ_H for the constant conductivity cases was approximately 0.6, whereas that for the variable conductivity case was about unity, indicating an approximate angle of 45 deg between the current and the electric field.

For trace concentrations of potassium, the electrical conductivity varies linearly with the potassium concentration, whereas the remaining physical and transport properties are essentially independent. Consequently, the plasma seedant can be scaled from this 1% level to provide the conductivity levels desired. This scaling has not been incorporated in the present calculations.

An overall view of pressure and Mach number variation in the channel is shown on Fig. 5 as a function of the external magnetic field for a variety of different load currents. (These computations correspond to the temperature-dependent conductivity case.) Figure 5a shows the pressure ratio (exit static to inlet total pressure) across the channel, whereas Fig. 5b shows the exit Mach number. The inlet Mach number was fixed at 2.0 for all cases. In general, the pressure drop increases and the exit Mach number decreases as the external magnetic field is increased. The load current has only a minor effect.

Cross-sectional cuts through the plasma and channel wall comparing the local current density in the fixed and variable conductivity cases are shown in Figs. 6 and 7. As already noted, the 1% potassium concentration results in a conductivity that is considerably below that for the constant conductivity (15 mho/m) case, giving rise to a weaker interaction between the plasma and the magnetic field in the temperature-dependent calculations. Most of the differences between the two solutions arise from this difference in magnitude of the conductivity rather than from its variation over the domain. We, however, note that the present calculations are done for an elevated wall temperature so that the significant effects of the plasma sheath created near the wall are bypassed. Continuum, steady calculations require a model for the sheath current,[10,11] but such a model has not been incorporated in the present calculations. The electrical current for both calculations is 1500 A.

Figure 6 shows the magnitude of the current density for a cross-sectional plane that crosses between the first conductor and the second dielectric ring. A schematic showing the location is given on the top of Fig. 6. The upper portion of this plane lies just after the entrance to the second dielectric ring, whereas its lower portion lies between the first and second rings. The current at this location is

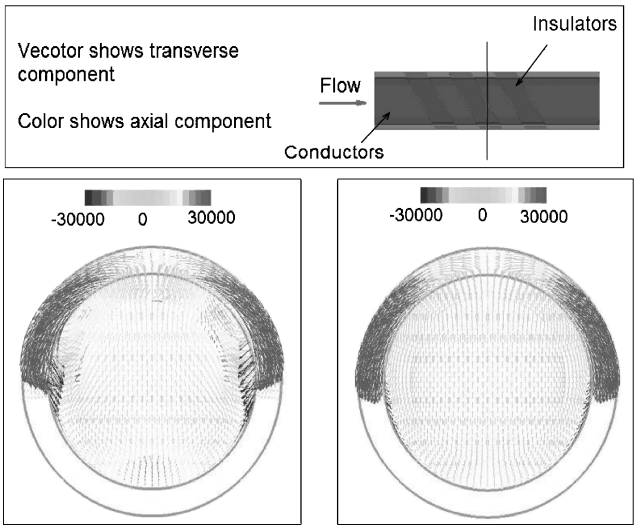

Fig. 7 Current density in plasma and channel wall at axial location $z = 0$ m, $B = 2$ T, $I = 1500$ A: left, constant conductivity, 15 mho/m and right, Equilibrium conductivity.

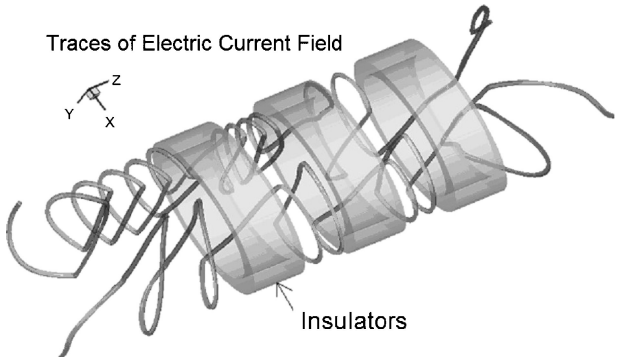

Fig. 8 Traces of individual current pathlines in channel with three skewed dielectric sections.

highly concentrated in the conductor at the bottom of the channel, whereas the insulator at the top contains no current. The results also show a weak current across the channel from the bottom to the top as the current from the lower conductor travels across the plasma to the next (third) conductor section at the top.

The variable and constant conductivity cases give qualitatively similar currents, although small variations are present. In particular, the current density in the bottom portion of the conductor is smaller for the variable conductivity case than for the constant conductivity case. Analogous current density results for a cross-sectional plane that cuts through the second dielectric ring and the third conductor are shown in Fig. 7 for an axial position just downstream of that in Fig. 6. At this second location, the conducting and dielectric portions of the channel wall are opposite to those in Fig. 7, and the current density is likewise approximately inverted from the results in Fig. 6. Here the plasma current again flows from bottom to top, and the current is seen entering the conductor at the top of the channel as it completes its cross-channel traverse. We also note that there is a considerable difference between the constant and variable conductivity cases at this axial plane. The constant conductivity case (on the left) shows much more local current near the midplane and less current in the middle of the channel. Again, these differences are more caused by a decreased level of conductivity on the right than the effects of cross-stream variations.

As a final look at this generator case, we present in Fig. 8 a three-dimensional view of the plasma with the locations of the dielectric rings superimposed in gray. The ribbons in Fig. 8 show traces of individual current pathlines inside the channel and conductors and give an idea of the manner in which they are skewed by the three

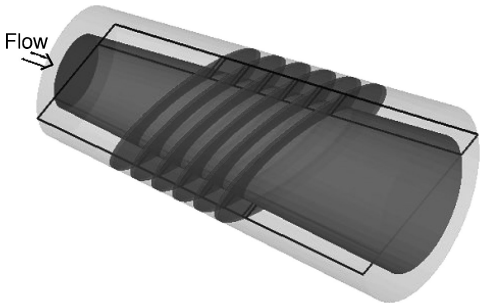

Fig. 9 Geometry for conical plasma channel.

dielectric sections. Clearly, the resulting current paths are highly three dimensional, and paths at various locations differ considerably from each other.

Conical Channel MHD Generator

As a second example of MHD computations, we present results for a conical channel whose area increases in the axial direction to counter flow deceleration effects created by removing energy from the flow. The geometry of this model is shown in Fig. 9, and a representative grid is given in Fig. 1. At the inlet, the inner and outer radii are 0.0445 and 0.0785 m, respectively, whereas at the outlet they are 0.0826 and 0.117 m. The channel length is 0.45 m. The channel contains six dielectric slabs oriented at an angle of 45 deg with respect to the axis. Each dielectric section has an axial extent of 0.005 m. The axial extent of the conductor between each dielectric slab is 0.025 m. The axial position of the six dielectric layers is shown in Fig. 9.

The computational domain is chosen to include the surrounding quiescent air out to a radius of 0.347 m. This radius should be large enough that the outer boundary condition has no impact on the solution. A total of 319,200 unstructured hexahedral grids (Fig. 1) has been used for these computations.

The flow conditions corresponding to this geometry again used an $M = 2$ condition at the inlet with an inlet static pressure of 4 atm and an inlet temperature of 2940 K. Computations have been done for a load current of $I = 5000$ A and two external magnetic field conditions placed across the channel. One B-field distribution is uniform in the axial direction with a magnitude of $B_0 = 2$ T. The other has an exponential variation in the axial direction given by $B_0 = 2\exp\lfloor -(2x/L - 1)^4/0.2\rfloor$, where L is the length of the channel. This distribution was chosen to simulate the expected axial falloff in an actual magnetic field. In the following discussion, we use the subscript uni to denote the uniform magnetic field case and exp for the exponential distribution case.

The Mach number distribution in the diverging channel is given in Fig. 10. Here the cross-sectional distribution is taken as longitudinal cuts through the channel for two planes 90 deg apart. Figure 10a is for the y–z plane that is parallel to the external magnetic field. In this plane the dielectric rings (which are also shown in Fig. 10) are inclined at an angle of 45 deg. Figure 10b shows the x–z plane that is normal to the B field. The dielectric rings are horizontal in this plane. Contours for both the uniform and exponential magnetic field cases are shown. The flooded contours correspond to the uniform magnetic field case. The gray contour lines superimposed on the flooded contours show the corresponding Mach number distribution for the exponential magnetic field.

The contours show that the Mach number increases in the flow direction for both magnetic fields indicating that the effect of channel divergence more than compensates for the power extraction. Starting from an inlet value of $M = 2.0$, the uniform magnetic field case increases to an exit Mach number of about 2.7, whereas the exponential field case increases to about 2.8. The larger Mach number increase in the exponentially varying field case arises because it has a weaker total magnetic field. The peak field is the same in both cases, but the exponential field drops off near both the inlet and the exit. The stronger uniform field case, thus, results in a smaller Mach

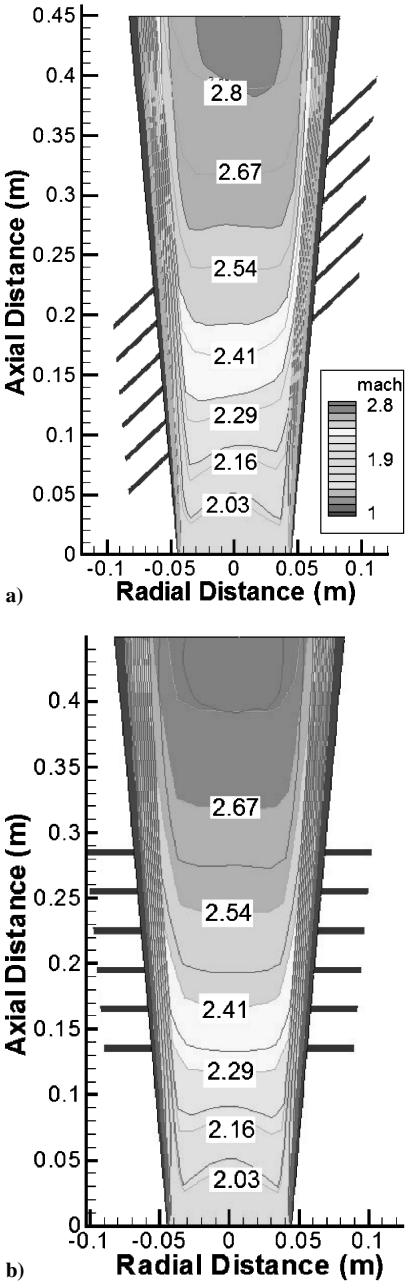

Fig. 10 Mach number contours in channel: upper, *y–z* plane (parallel to magnetic field); lower, *x–z* plane (normal to magnetic field); flooded contours, uniform magnetic field; and superimposed gray contour lines, exponential magnetic field.

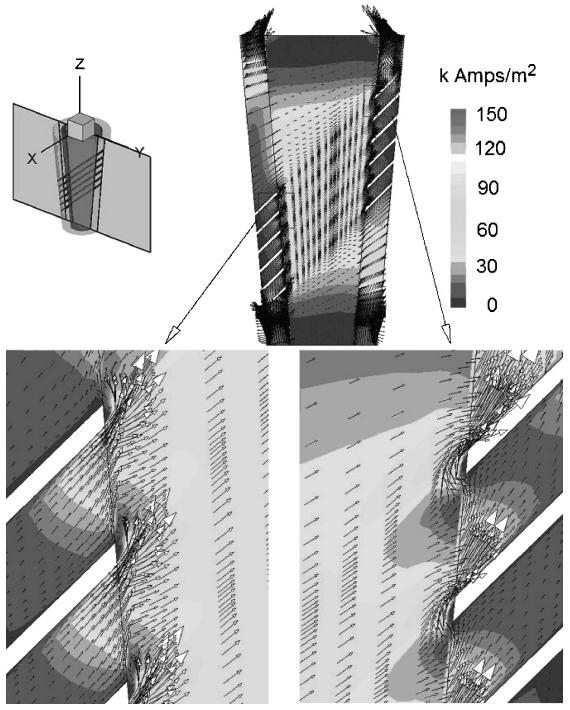

Fig. 11 Electrical current density and tangential current vectors in channel walls and plasma for *y–z* plane on channel centerline, *x* = 0 m; bottom, blowup of wall region on either side near the last dielectric slab.

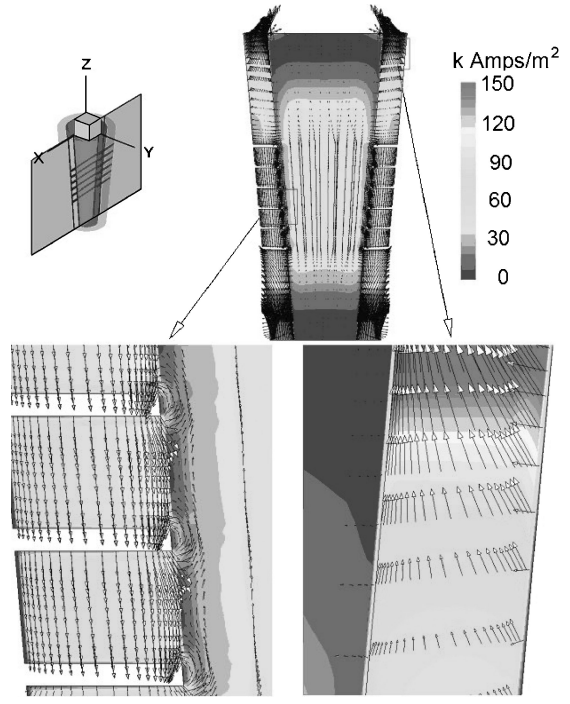

Fig. 12 Electrical current density and tangential current vectors in channel walls and plasma for *x–z* plane on the channel centerline, *y* = 0 m; bottom, details of current in the middle of the dielectric slabs (left) and near the outlet plane (right).

number increase than the weaker varying field case. In both cross planes, the contours are approximately aligned with the dielectric rings. In Fig. 10a where the dielectrics are skewed at 45 deg, the contours are likewise skewed, while in Fig. 10b where the dielectric rings are symmetric, the contours are also nearly symmetric.

In addition to the plane through the center of the tube, two local regions, both showing details of the electrical field in the vicinity of the sixth dielectric slab near the intersection between the plasma, the conductor and the dielectric, are given at the bottom of Fig. 11. Note that the local plots in Fig. 11 show that a portion of the current that leaves the conductor as it approaches an insulator travels across the plasma to enter the conducting portion on the opposite side. In addition, there is also evidence that a substantial amount of the current enters the plasma, jumps across the dielectric slab, and reenters the conductor adjacent to the location at which it left. This direct reentry is much larger for these thin dielectric slabs than for the thicker ones analyzed earlier and suggests the possibility that arcing can be generated across the dielectric. We note that the present computations are on a relatively coarse grid so that these results must be interpreted qualitatively rather than quantitatively. Extending the model to finer grids to study local phenomena such as these is readily accomplished, but present resources preclude it.

Figure 12 shows analogous results for the *x–z* plane rotated 90 deg from the cutting plane given in Fig. 11. Again, local views of conditions in the conductor, plasma, and dielectric regions near the middle of the channel are given, along with detail of the conductor

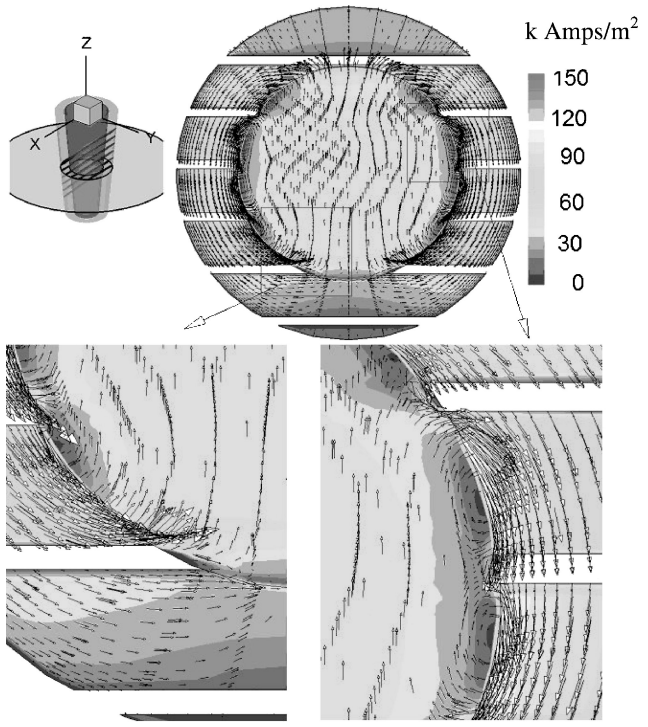

Fig. 13 Electrical current density and tangential current vectors in channel walls and plasma for x–y plane on the plane $z = 0.20$ m.

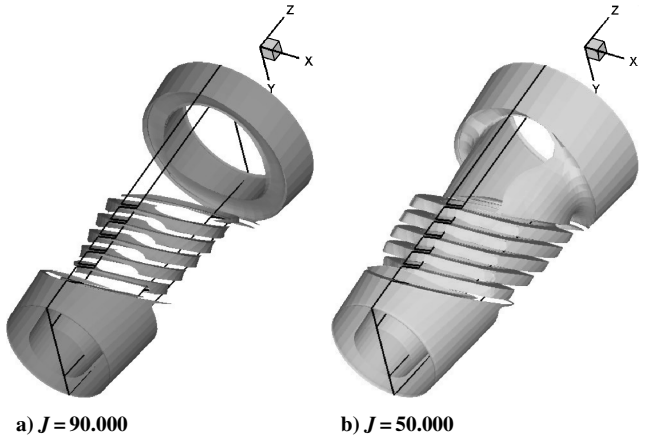

a) $J = 90.000$ **b) $J = 50.000$**

Fig. 14 Isosurfaces of electrical current density.

region near the outlet plane. Note that the views in this plane give a much different perspective on the electric field than the previous plane. Again, there is substantial evidence of a sheath layer near the dielectric slabs. Figure 13 shows the calculation at an x–y plane at axial location $z = 0.2$ m, along with a local detailed look near the plasma, dielectric and conductor intersection.

Figures 14a and 14b show the isosurfaces of the current density magnitude for values $J = 90{,}000$ and $50{,}000$ A/m^2. These surfaces show that the current distribution in the conductor is very nonuniform due to the dielectric rings and the induced magnetic field.

Summary

The detailed characteristics of the three-dimensional current and fluid flow in diagonally connected MHD generators are studied by numerical solutions. The magnetic induction equation is solved in conjunction with the Reynolds averaged Navier–Stokes equations and a two-equation turbulence model by means of a flux-split upwind method employing an unstructured grid methodology. A generalized Ohm's law is used to include Hall effects that are important at the conditions of interest. Boundary conditions for the fluid are specified on the channel walls, whereas boundary conditions for the magnetic diffusion equation are specified on a cylindrical domain whose radius is large compared to the channel where physically realistic conditions can easily be deduced. The combined solution, therefore, gives the current distribution in the plasma and the conducting portions of the channel wall.

Details of the power generated by a mixture of hot combustion gases and a trace amount of potassium are presented for generators with both constant and diverging area channels. All cases considered are for supersonic flow. The results show very intricate current paths through the channel as the current moves from the conductor to the plasma and back again into the conductor to avoid the dielectric sectors. When the streamwise extent of the dielectric strips is relatively large, nearly all of the current flows across the channel to the opposite wall. As the width of the strips is decreased, a significant portion of the current jumps across the insulator and re-enters the conductor without crossing the channel. The results for the constant area channel show the expected decrease in Mach number as the external magnetic field is increased, whereas Mach number in the diverging area cases continue to increase, indicating that the effects of area divergence more than offset the effects of power extraction.

Appendix: Eigenvectors of Jacobian Matrix

The left and right eigenvectors of Eq. (18) are

$$M = \begin{pmatrix} 0 & 0 & 0 & 0 & 0 & \frac{\rho^2 h_T}{\Delta} & \frac{\rho^2 h_T}{\Delta} & \frac{\rho^2 h_T}{\Delta} & \frac{\rho^2 h_T}{\Delta} \\ 0 & 1 & 0 & 0 & 0 & 0 & 0 & 0 & 0 \\ \mathbf{0} & \mathbf{0} & \mathbf{0} & \alpha & \alpha & \boldsymbol{W}_f & -\boldsymbol{W}_f & \boldsymbol{W}_s & -\boldsymbol{W}_s \\ \frac{1}{\rho_T} & 0 & 0 & 0 & 0 & \frac{\beta}{\Delta} & \frac{\beta}{\Delta} & \frac{\beta}{\Delta} & \frac{\beta}{\Delta} \\ \mathbf{0} & \mathbf{0} & \boldsymbol{n} & -\alpha\sqrt{\rho\mu_0} & \alpha\sqrt{\rho\mu_0} & \boldsymbol{M}_f & \boldsymbol{M}_f & \boldsymbol{M}_s & \boldsymbol{M}_s \end{pmatrix}$$

$$M^{-1} = \begin{pmatrix} \frac{\rho_p - 1}{a^2} & 0 & \mathbf{0} & \rho_T & \mathbf{0} \\ 0 & 1 & \mathbf{0} & 0 & \mathbf{0} \\ 0 & 0 & \mathbf{0} & 0 & \boldsymbol{n} \\ 0 & 0 & \alpha & 0 & \frac{-\alpha}{\sqrt{\rho\mu_0}} \\ 0 & 0 & \alpha & 0 & \frac{\alpha}{\sqrt{\rho\mu_0}} \\ \frac{1}{G_f} & 0 & \frac{\rho \boldsymbol{W}_f}{G_f} & 0 & \frac{\boldsymbol{M}_f}{G_f \mu_0} \\ \frac{1}{G_f} & 0 & \frac{-\rho \boldsymbol{W}_f}{G_f} & 0 & \frac{\boldsymbol{M}_f}{G_f \mu_0} \\ \frac{1}{G_s} & 0 & \frac{\rho \boldsymbol{W}_s}{G_s} & 0 & \frac{\boldsymbol{M}_s}{G_s \mu_0} \\ \frac{1}{G_s} & 0 & \frac{-\rho \boldsymbol{W}_s}{G_s} & 0 & \frac{\boldsymbol{M}_s}{G_s \mu_0} \end{pmatrix}$$

where

$$\alpha = \frac{\boldsymbol{n} \times \boldsymbol{B}}{\sqrt{2\left(\boldsymbol{B} \cdot \boldsymbol{B} - B_n^2\right)}}, \qquad \beta = \rho(1 - \rho h_p)$$

$$\boldsymbol{W}_{f,s} = \frac{c_{f,s}\left(B_n^2 \boldsymbol{n} - B_n \boldsymbol{B}\right)}{\rho\mu_0 c_{f,s}^2 - B_n^2} + c_{f,s}\boldsymbol{n}$$

$$\boldsymbol{M}_{f,s} = \frac{\rho\mu_0 c_{f,s}^2 (\boldsymbol{B} - B_n \boldsymbol{n})}{\rho\mu_0 c_{f,s}^2 - B_n^2}$$

$$G_{f,s} = 2\left[\frac{\rho^2 h_T}{\Delta} + \frac{\boldsymbol{B}\cdot\boldsymbol{B} - B_n^2}{\mu_0}\left(\frac{\rho\mu_0 c_{f,s}^2}{\rho\mu_0 c_{f,s}^2 - B_n^2}\right)^2\right]$$

$$= 2\left(\frac{\rho^2 h_T}{\Delta} + \frac{\boldsymbol{M}_{f,s}\cdot\boldsymbol{M}_{f,s}}{\mu_0}\right)$$

These eigenvectors are generalized, orthonormal, and well defined except in the limit when $\boldsymbol{B}\cdot\boldsymbol{B} - B_n^2 = 0$, in which case $\boldsymbol{n}\times\boldsymbol{B}/\sqrt{\boldsymbol{B}\cdot\boldsymbol{B} - B_n^2}$ approaches 0/0 and can be treated by the procedure proposed by Roe and Balsara,[7] where the quantity $\boldsymbol{n}\times\boldsymbol{B}/\sqrt{\boldsymbol{B}\cdot\boldsymbol{B} - B_n^2}$ is set equal to one.

Acknowledgement

This work was supported by General Atomics under Contract SCDC 123501.

References

[1]Sutton, G. W., and Sherman, A., *Engineering Magnetohydrodynamics*, McGraw–Hill, New York, 1965, pp. 471–482.

[2]Li, D., and Merkle, C. L., "Convergence Assessment of General Fluid Equation on Unstructured Hybrid Grids," AIAA Paper 2001-2557, June 2001.

[3]Li, D., and Merkle, C. L., "CFD Analysis of Leakage Characteristics of Labyrinth Seals in a Steam Turbine," American Society of Mechanical Engineers, Fluids Engineering Div. Summer Meeting Paper FEDSM2001-18060, Aug. 2001

[4]Powell, K. G., Roe, P. L., Myong, R. S., Gombosi, T., and De Zeeuw, D. L., "An Upwind Scheme for Magnetohydrodynamics," *Proceedings of the 12th AIAA Computational Fluid Dynamics Conference*, AIAA, Washington, DC, June 1995, pp. 661–672.

[5]Powell, K. G., Tóth, G., De Zeeuw, D. L., Roe, P. L., Gombosi, T. I., and Stout, Q. F., "Development and Validation of Solution-Adaptive, Parallel Schemes for Compressible Plasmas," *Proceedings of the 15th AIAA Computational Fluid Dynamics Conference*, AIAA, Reston, VA, June 2001, pp. 1–10.

[6]Wilcox, D. C., *Turbulence Modeling for CFD*, Kni, Inc., Anaheim, CA, 1998.

[7]Roe, P. L., and Balsara, D. S., "Notes on the Eigensystem of Magnetohydrodynamics," *SIAM Journal on Applied Mathematics*, Vol. 56, No. 1, 1996, pp. 57–67.

[8]Frese, M., "MACH2: A Two-Dimensional Magnetohydrodynamic Simulation Code for Complex Experimental Configurations," Mission Research Corp., Technical Rept. AMRCP-814, Albuquerque, NM, Sept. 1987.

[9]Bouillard, J. X., Krazinski, J. L., Vanka, S. P., and Berry, G. F., "Performance of a Multigrid Three Dimensional MHD Generator Calculation Procedure," *Proceedings of the 27th Symposium on the Engineering Aspects of Magnetohydrodynamics*, June 1989, pp. 5.2.1–5.2.12.

[10]Choueiri, E. Y., "Anomalous Resistivity and Heating in Current-Driven Plasma Thrusters," *Physics of Plasmas*, Vol. 6, No. 5, 1999, pp. 2290–2306.

[11]Niewood, E. H., "An Explanation for Anode Voltage Drops in an MPD," M.S. Thesis, Massachusetts Inst. of Technology, Cambridge, MA, 1993.